Science
AAAS

Supplementary Materials for

Gate-tunable negative refraction of mid-infrared polaritons

Hai Hu *et al*.

Corresponding authors: Hai Hu, huh@nanoctr.cn; F. Javier García de Abajo, javier.garciadeabajo@nanophotonics.es; Qing Dai, daiq@nanoctr.cn

Science **379**, 558 (2023)
DOI: 10.1126/science.adf1251

The PDF file includes:

Materials and Methods

Nanofabrication of the devices.

The α-$RuCl_3$/graphene/α-MoO_3 heterostructures were exfoliated and stacked using a vdW assembly technique (fig. S6). Initially, monolayer α-$RuCl_3$ (Shanghai Onway Technology Co., Ltd.), monolayer graphene, and α-MoO_3 films (~242 nm) were taken from natural crystals and exfoliated on SiO_2 (300 nm)/Si and Au (60 nm)/Si substrates, respectively. Then, α-$RuCl_3$ and graphene were picked up by a deterministic dry-transfer process aided by a glass /polydimethylsiloxane (PDMS)/polycarbonate (PC) stamp at 100 ℃. After that, the stamp with α-$RuCl_3$ /graphene was aligned with α-MoO_3 and the temperature was raised to 180 ℃ to release the heterostructure with PC and form α-$RuCl_3$/graphene/α-MoO_3 heterostructures. The samples were subsequently immersed in chloroform for 10 min and rinsed in IPA for 3 min to eliminate any residual PC. The double-layer graphene involved in Fig. 3 of the main text also uses the above method to randomly stack two layers of mechanically exfoliated single-layer graphene. We note that monolayer α-$RuCl_3$ has been reported to produce high and homogeneous doping in monolayer graphene with mobilities ~4900 $cm^2/(V\cdot s)$ at a large hole density of 2.7×10^{13} cm^{-2}, while having minimal optical absorption in the mid-infrared range (*39*).

The Au antennas (3 μm × 250 nm × 50 nm) were patterned on the sample using 100 kV electron-beam lithography (EBL) (Vistec 5000+ES, Germany) on PMMA950K resist (thickness of ~350 nm). After that, a layer of 50 nm thickness of Au was deposited by electron-beam evaporation in a vacuum chamber under a pressure of 5×10^{-6} Torr. We deliberately did not prepare an adhesion layer (usually 5 nm thickness of Ti or Cr), so that the gold antennas on the sample could be moved away by an AFM tip (fig. S7). Electron-beam evaporation was also used to deposit a 60 nm-thick gold film onto a low-doped Si substrate. To remove any residual organic materials, the samples were immersed in a hot acetone bath at 80 °C for 25 min and subject to a gentle rinse of IPA for 3 min, followed by nitrogen gas drying and thermal baking.

Near-field optical microscopy measurements.

For near-field measurements, a scattering SNOM setup (Neaspec GmbH) equipped with a tunable quantum cascade laser (890 to 2000 cm^{-1}) was utilized. A Pt-coated AFM tip with a radius of ~25 nm (NanoWorld) was employed, with a tapping frequency and amplitude of ~270 kHz and ~30-50 nm, respectively. A *p*-polarized mid-infrared beam with a lateral spot size of 25 μm was aimed

at the AFM tip, illuminating the antennas and a large area of the graphene/α-MoO_3 samples. To effectively reduce background noise, a third-order demodulated-harmonic analysis (S_3 (ω)) of the near-field amplitude images was applied.

Calculation of dispersion and IFCs of hybrid plasmon-phonon polaritons.

The dispersion of hybrid polaritons was obtained from waveguide theory applied to graphene/α-MoO_3 heterostructure, in which the structure was modeled as a 2D waveguide consisting of four stacked layers (see more details in fig. S3 and Note S2). In this analysis, air and the gold substrate were modeled in terms of their isotropic dielectric tensors, while α-MoO_3 was described by anisotropic tensors.

Electromagnetic simulations.

A Finite Element Method software (COMSOL Multiphysics 5.5) was used to simulate the electromagnetic field. The model was constructed by following the geometrical specifications in the experimental samples, in which graphene was described as a 0.33-nm-thick transition interface, the metallic antenna was placed on the graphene/α-MoO_3 sample, and the substrate was a 60-nm-thick gold film. Perfectly matched layers were set up at all boundaries around the model to reduce boundary reflections. The incident light was set as a plane wave polarized along the long axis of the antenna with an angle of 45º to the surface. To simulate the tip-launched polaritons, we introduced a dipole located 100 nm above the surface and polarized perpendicular to the surface. The electric field distribution was calculated on a plane situated 20 nm above the uppermost surface of the sample. To simplify the simulation, we ignored the single layer of α-$RuCl_3$. This approximation should have a negligible effect on the simulation outcomes, as a single layer of α-$RuCl_3$ would only introduce a small dielectric loss (fig. S21).

Note S1. Optical parameters of graphene and α-MoO_3.

In our work, graphene is modeled as a homogenous two-dimensional conducting layer, and the conductivity σ can be modeled in the local limit of the random-phase approximation (RPA) and decomposed into intra-band and inter-band contributions as (*40*)

$$\sigma(\omega) = \frac{ie^2 K_B T\left(\omega+\frac{1}{\tau}\right)}{\pi\hbar^2}\left[\frac{E_F}{K_B T} + 2\ln\left(\exp\left(-\frac{E_F}{K_B T}\right)+1\right)\right] + i\frac{e^2}{4\pi\hbar}\ln\left[\frac{2|E_F|-\hbar\left(\omega+\frac{i}{\tau}\right)}{2|E_F|+\hbar\left(\omega+\frac{i}{\tau}\right)}\right], \qquad (S1)$$

which depends on the Fermi energy E_F, the temperature T, and the relaxation time $\tau = \mu E_F / ev_F^2$, expressed in terms of the graphene Fermi velocity $v_F = c/300$ and the carrier mobility μ. The latter is assumed to be 4900 $cm^2\ V^{-1}\ s^{-1}$. The real and imaginary parts of the graphene conductivity as a function of the Fermi energy and frequency are plotted in fig. S1.

The permittivity of α-MoO_3 can be modeled by the Lorentz model (*26*)

$$\varepsilon_j = \varepsilon_\infty^j\left(1 + \frac{{\omega_{LO}^j}^2 - {\omega_{TO}^j}^2}{{\omega_{TO}^j}^2 - \omega^2 - i\omega\gamma^j}\right), \qquad j = x, y, z \qquad (S2)$$

where ε_j denotes the principal components of the permittivity tensor of α-MoO_3. The parameters ε_∞^j are the high-frequency dielectric constants along the directions j, while ω_{LO}^j and ω_{TO}^j refer to the LO and TO phonon frequencies, respectively. The parameters γ^j are inelastic loss rates of the material. The coordinates *x*, *y*, and *z* are oriented along the three principal axes of the crystal, which correspond to the crystallographic directions [100], [001], and [010] of α-MoO_3, respectively. Detailed parameters are shown in Table S1. The real and imaginary parts of the α-MoO_3 permittivity along the three principal axes are plotted in fig. S1.

Table S1. Parameters used for modeling the permittivity of α-MoO_3.

Direction	$\boldsymbol{\varepsilon_\infty}$	$\boldsymbol{\omega_{LO}}$ (cm^{-1})	$\boldsymbol{\omega_{TO}}$ (cm^{-1})	$\boldsymbol{\gamma}$ (cm^{-1})
x [100]	4	972	820	4
y [001]	5.2	851	545	4
z [010]	2.4	1004	958	2

Note S2. Calculation of the dispersion and IFCs of hybrid plasmon-phonon polaritons.

In the theoretical model, we treat the graphene/α-MoO_3 heterostructure as a laterally-infinite stratified medium consisting of four layers (fig. S3): $z > 0$ (air, layer 1), $-d_1 < z < 0$ (graphene, layer 2), $-d_2 < z < -d_1$ (α-MoO_3, layer 3), and $z < -d_2$ (Au, layer 4). Each layer is represented by its corresponding dielectric tensor. The air and Au layers are described by isotropic tensors $\mathrm{diag}\{\varepsilon_{a,s}\}$, while graphene is modeled as a uniaxial anisotropic material (*41*), whose permittivity tensor is given by

$$\bar{\bar{\varepsilon}}_{graphene} = \begin{bmatrix} \varepsilon_{gt} & 0 & 0 \\ 0 & \varepsilon_{gt} & 0 \\ 0 & 0 & \varepsilon_{gz} \end{bmatrix}, \quad (S3)$$

where the tangential permittivity is expressed as

$$\varepsilon_{gt} = 1 + i\frac{i\sigma}{\omega\varepsilon_0 t_g} \quad (S4)$$

while the out-of-plane permittivity is set to

$$\varepsilon_{gz} = 1. \quad (S5)$$

Here, ε_0 is the free-space permittivity, t_g represents the thickness of monolayer graphene, which is set to 0.33 nm, and σ represents the optical conductivity of graphene taken from the local limit of the RPA (following Eq. ($S1$)).

As α-MoO_3 is a biaxial anisotropic material, its permittivity tensor is modeled as

$$\bar{\bar{\varepsilon}}_{\mathrm{MoO_3}} = \begin{bmatrix} \varepsilon_{mx} & 0 & 0 \\ 0 & \varepsilon_{my} & 0 \\ 0 & 0 & \varepsilon_{mz} \end{bmatrix}, \quad (S6)$$

where ε_{mx}, ε_{my}, and ε_{mz} are the permittivity components along the principal axes (as shown in Note S1 and fig. S1).

Without loss of generality, we consider polariton waves propagating with an in-plane wave vector $\vec{k}_{in-plane} = (k_x, k_y)$, such that

$$k_x = k_{\mathrm{in-plane}}\cos(\psi), \qquad k_y = k_{\mathrm{in-plane}}\sin(\psi), \quad (S7)$$

where ψ denotes the angle between $\vec{k}_{\mathrm{in-plane}}$ and the *x* axis.

Through a simple coordinate transformation, the dielectric function of α-MoO_3 along the direction of wave propagation $\vec{k}_{\mathrm{in-plane}}$ can be expressed as $\varepsilon_{mt} = \varepsilon_{mx}\,cos^2(\psi) + \varepsilon_{my}\,sin^2(\psi)$, and thus,

we find a 2D dielectric function diag $\{\varepsilon_{mt}, \varepsilon_{mz}\}$. Similarly, we can write the graphene permittivity tensor as diag $\{\varepsilon_{gt}, \varepsilon_{gz}\}$.

In our system, the α-MoO_3 layer contains TM-TE mixed modes, but the weight of the TE component is much weaker than the TM one (*28*). As an approximation, we consider TM modes in the following derivation. We focus on a 2D waveguide mode with $\vec{k}_{\mathrm{in-plane}}$ directed along the *x* axis, as shown in fig. S3. The transverse magnetic field in the graphene/α-MoO_3 heterostructure can be expressed as $\vec{H}_y = H_y(z)\exp(iqx - \omega t)\,\vec{e}_y$, where $q = |\vec{k}_{in-plane}|$ and $\vec{e}_y$ is the unit vector along y. Solving the wave equation $\nabla^2\vec{H} + k_0^2\,\bar{\bar{\varepsilon}}\vec{H} = \nabla(\nabla\cdot\vec{H})$ in each layer, we find the relations

$$\frac{\partial^2\vec{H}_y}{\partial z^2} + \left(k_0^2\varepsilon_{a,s} - q^2\right)\vec{H}_y = 0, \qquad (S8)$$

$$\frac{\partial^2\vec{H}_y}{\partial z^2} + \left(k_0^2\varepsilon_t^{(j)} - \left(\frac{\varepsilon_t^{(j)}}{\varepsilon_z^{(j)}}\right)q^2\right)\vec{H}_y = 0, \qquad (S9)$$

where *j* = 2 and *j* = 3 denote the graphene and α-MoO_3 layers, respectively. For a van der Waals structure of finite thickness, the solution for $H_y(z)$ can be expressed as

$$H_y(z) = \begin{cases} (A+B)e^{-\alpha_a z} & (z > 0), \\ Ae^{ik_z^{(2)}z} + Be^{-ik_z^{(2)}z} & (-d_1 < z \le 0), \\ Ce^{ik_z^{(3)}z} + De^{-ik_z^{(3)}z} & (-d_2 < z \le -d_1), \\ \left(Ce^{-ik_z^{(3)}d_2} + De^{ik_z^{(3)}d_2}\right)e^{\alpha_s(z+d_2)} & (z \le -d_2). \end{cases} \qquad (S10)$$

Here, $\alpha_{a,s} = \sqrt{q^2 - k_0^2\varepsilon_{a,s}}$ is the out-of-plane decay coefficient of the air layer (*j* = 1, α_a) and Au layer (*j* = 4, α_s), while $k_z^{(j)} = \sqrt{k_0^2\varepsilon_t^{(j)} - \left(\frac{\varepsilon_t^{(j)}}{\varepsilon_z^{(j)}}\right)q^2}$ is the normal wave vector component in the graphene (*j* = 2) and α-MoO_3 (*j* = 3) layers. The four unknown parameters *A*, *B*, *C*, and *D* are the amplitude coefficients of the nontrivial solution that is found by matching the electromagnetic boundary conditions and imposing the vanishing of the associated secular determinant. In addition, d_1 and d_2 are the thicknesses of the graphene (*j* = 2) and α-MoO_3 (*j* = 3) layers, respectively.

To find $\vec{E}_x = E_x(z)\exp(iqx - \omega t)\,\vec{e}_x$, we plug H_y into the curl equation $\nabla \times H = i\omega\varepsilon_0\bar{\bar{\varepsilon}}E$. We obtain

$$E_x(z)=\begin{cases}\dfrac{i\alpha_a}{\omega\varepsilon_0\varepsilon_a}(A+B)e^{-\alpha_a z} & (z>0),\\ \dfrac{1}{\omega\varepsilon_0\varepsilon_t^{(2)}}\left(Ak_z^{(2)}e^{ik_z^{(2)}z}-Bk_z^{(2)}e^{-ik_z^{(2)}z}\right) & (-d_1<z\le 0),\\ \dfrac{1}{\omega\varepsilon_0\varepsilon_t^{(3)}}\left(Ck_z^{(3)}e^{ik_z^{(3)}z}-Dk_z^{(3)}e^{-ik_z^{(3)}z}\right) & (-d_2<z\le -d_1),\\ \dfrac{-i\alpha_s}{\omega\varepsilon_0\varepsilon_s}\left(Ce^{-ik_z^{(3)}d_2}+De^{ik_z^{(3)}d_2}\right)e^{\alpha_s(z+d_2)} & (z\le -d_2).\end{cases} \quad (S11)$$

Considering that the tangential components of $\vec{E}$ and $\overrightarrow{H}$ are continuous at the interface, we find the following equations

$$\begin{cases}E_x^{(1)}=E_x^{(2)}, H_y^{(1)}=H_y^{(2)}, & z_1=0,\\ E_x^{(2)}=E_x^{(3)}, H_y^{(2)}=H_y^{(3)}, & z_2=-d_1,\\ E_x^{(3)}=E_x^{(4)}, H_y^{(3)}=H_y^{(4)}, & z_3=-d_2.\end{cases} \quad (S12)$$

By substituting the fields in Eqs. ($S10$) and ($S11$) into the boundary conditions, we obtain the secular matrix equation

$$\begin{bmatrix}\dfrac{i\alpha_a}{\varepsilon_a}-\dfrac{k_z^{(2)}}{\varepsilon_t^{(2)}} & \dfrac{i\alpha_a}{\varepsilon_a}+\dfrac{k_z^{(2)}}{\varepsilon_t^{(2)}} & 0 & 0\\ \dfrac{k_z^{(2)}}{\varepsilon_t^{(2)}}e^{-ik_z^{(2)}d_1} & -\dfrac{k_z^{(2)}}{\varepsilon_t^{(2)}}e^{ik_z^{(2)}d_1} & -\dfrac{k_z^{(3)}}{\varepsilon_t^{(3)}}e^{-ik_z^{(3)}d_1} & \dfrac{k_z^{(3)}}{\varepsilon_t^{(3)}}e^{ik_z^{(3)}d_1}\\ e^{-ik_z^{(2)}d_1} & e^{ik_z^{(2)}d_1} & -e^{-ik_z^{(3)}d_1} & e^{ik_z^{(3)}d_1}\\ 0 & 0 & \left(\dfrac{i\alpha_s}{\varepsilon_s}+\dfrac{k_z^{(3)}}{\varepsilon_t^{(3)}}\right)e^{-ik_z^{(3)}d_2} & \left(\dfrac{i\alpha_s}{\varepsilon_s}-\dfrac{k_z^{(3)}}{\varepsilon_t^{(3)}}\right)e^{ik_z^{(3)}d_2}\end{bmatrix}\begin{bmatrix}A\\B\\C\\D\end{bmatrix}=0. \quad (S13)$$

Denoting the square matrix in this equation by M, we impose the vanishing of the determinant det{M} = 0 to guarantee the existence of a nonzero solution for the amplitude coefficients *A*, *B*, *C*, and *D*. Such condition leads to the transcendental equation

$$e^{2p_1}=-\frac{[(p_2-p_3)(p_3-p_4)(p_4+p_5)]e^{ik_z^{(2)}d_1}+[(p_2+p_3)(p_3+p_4)(p_4+p_5)]e^{-ik_z^{(2)}d_1}}{[(p_2-p_3)(p_3+p_4)(p_4-p_5)]e^{ik_z^{(2)}d_1}+[(p_2+p_3)(p_3-p_4)(p_4-p_5)]e^{-ik_z^{(2)}d_1}}, \quad (S14)$$

where

$$
\begin{aligned}
p_1 &= -ik_z^{(3)} d_1 + ik_z^{(3)} d_2, \\
p_2 &= \frac{i\alpha_a}{\varepsilon_a}, \\
p_3 &= \frac{k_z^{(2)}}{\varepsilon_t^{(2)}}, \\
p_4 &= \frac{k_z^{(3)}}{\varepsilon_t^{(3)}}, \\
p_5 &= \frac{i\alpha_s}{\varepsilon_s}.
\end{aligned}
\tag{S15}
$$

The solution to Eq. ($S14$) yields the mode dispersion, which can be solved for each value of the angle ψ (see Eq. ($S7$)), thus generating a function $q(\psi)$ that can be understood as IFC of the polaritons. Following this procedure, we find the numerical results in Fig. 1B.

Note S3. Theoretical analysis of the focal position associated with negative refraction.

As the tangential wave vectors of the interface for the refraction process are continuous (this is essentially Snell's Law), the relationship between the incidence and refraction angles can be obtained numerically, as illustrated in fig. S5A.

For the bare α-MoO_3 film, the hyperbolic polaritons in the Reststrahlen band II (816~972 cm^{-1}) are highly oriented. When approaching the two asymptotes of the hyperbolic IFC, the number of available wave vectors of PhPs and the intensity of the electric field are significantly increased, as inferred upon examination of the Dyadic Green tensor (*42*). More precisely, the *zz* component of the Dyadic Green tensor of the bare α-MoO_3 film reduces to

$$G_{zz}(\mathbf{r}-\mathbf{r}') = \frac{\epsilon^{\frac{3}{2}}}{\sqrt{(\pi d)}} \frac{\left(\epsilon_x^2\Delta y^2 + \epsilon_y^2\Delta x^2\right)e^{-qk_0H}}{\epsilon_x^2\epsilon_y^{\frac{5}{4}}(k_0d)^2\left(\epsilon_x\Delta y^2 + \epsilon_y\Delta x^2\right)^{\frac{5}{4}}} \exp\left\{\frac{i\left(2\epsilon\sqrt{\epsilon_x\Delta y^2 + \epsilon_y\Delta x^2}\right)}{\epsilon_x\sqrt{\epsilon_y}d} - \frac{\pi}{4}\right\}, \quad (S16)$$

where

$$q = -\frac{2\epsilon\sqrt{\epsilon_x^2\Delta y^2 + \epsilon_y^2\Delta x^2}}{\epsilon_x\sqrt{\epsilon_y}k_0d\sqrt{\epsilon_x\Delta y^2 + \epsilon_y\Delta x^2}} \quad (S17)$$

denotes the in-plane wave vector and ϵ represents the relative dielectric function given by the average value of the upper and lower media. We take $\epsilon = 1$ and denote $\Delta r = |\mathbf{r} - \mathbf{r}'|$ the distance from the target point to the source point, with relative vector projections on the *x* and *y* directions given by Δx and Δy. In addition, k_0 represents the free-space wave vector of the incident light, *d* denotes the thickness of α-MoO_3, and *H* is the height of the detection point.

In fig. S5B, we plot the absolute value of $G_{zz}(r - r')$ (orange solid curve), obtained from Eq. ($S16$) as a function of polar angle at a distance $\Delta r = 2.5$ μm from the source point for an illumination frequency of 893 cm^{-1}. The thickness of α-MoO_3 is set at *t* = 240 nm. We set the monitoring point for the α-MoO_3 film at a height *H* = 50 nm. The pseudo-color map of the background is obtained from a numerical simulation of the electric-field absolute amplitude $|E_z|$ excited by a point electric dipole placed 100 nm above the α-MoO_3 surface. The near-field absolute amplitude shows a maximum at an angle φ_c with respect to the [100] crystal direction (set to *x* here), which indicates that energy is mainly canalized along this direction. We consider φ_c as the main angle sustained by the incident light, such that the intersection of the refraction angle corresponding to φ_f is calculated as the focal point. Using this simplified model, the relative positional relationship between the source and focal spot can be determined as follows,

$$d = f\,\frac{\tan(\varphi_c)}{\tan(\varphi_f)}, \qquad (S18)$$

where d and f represent the distance from the source point and the focal spot to the graphene edge, respectively.

Notably, the refraction angle in our structure has a finite range rather than being at a single fixed angle. As a result, these angular deviations cause some defocusing. However, since the distribution of such angular deviations is small (within ten degrees, Fig. S5B), the defocusing effect can roughly be ignored. Because of this, we can observe the focal point clearly in both experiments and simulations. In the future, optimization of the interface geometry could allow for corrections of the angles of all refracted beams, such that they point to the same direction, thus improving focusing performance.

In addition, the negative refraction approach to focusing is essentially different from the antenna shaping approach in a hyperbolic media. In particular, antenna shaping changes the light at the original source to achieve focusing (*41*, *43*, *44*); in contrast, negative refraction works by changing the propagation path of light which has been excited before, and finally produces focusing. As a result, negative refraction in this work has the benefits of focusing divergent waves that are already excited, manipulating focusing in situ, and enabling active control and dynamic switching to focus. It should be noted that by reducing the thickness of α-MoO_3 to the monolayer, the theoretical upper limit on the focusing linewidth can be significantly increased. Since phonon polaritons are mainly volume modes, the thickness of the material has an inverse relationship with how tightly they are constrained in space.

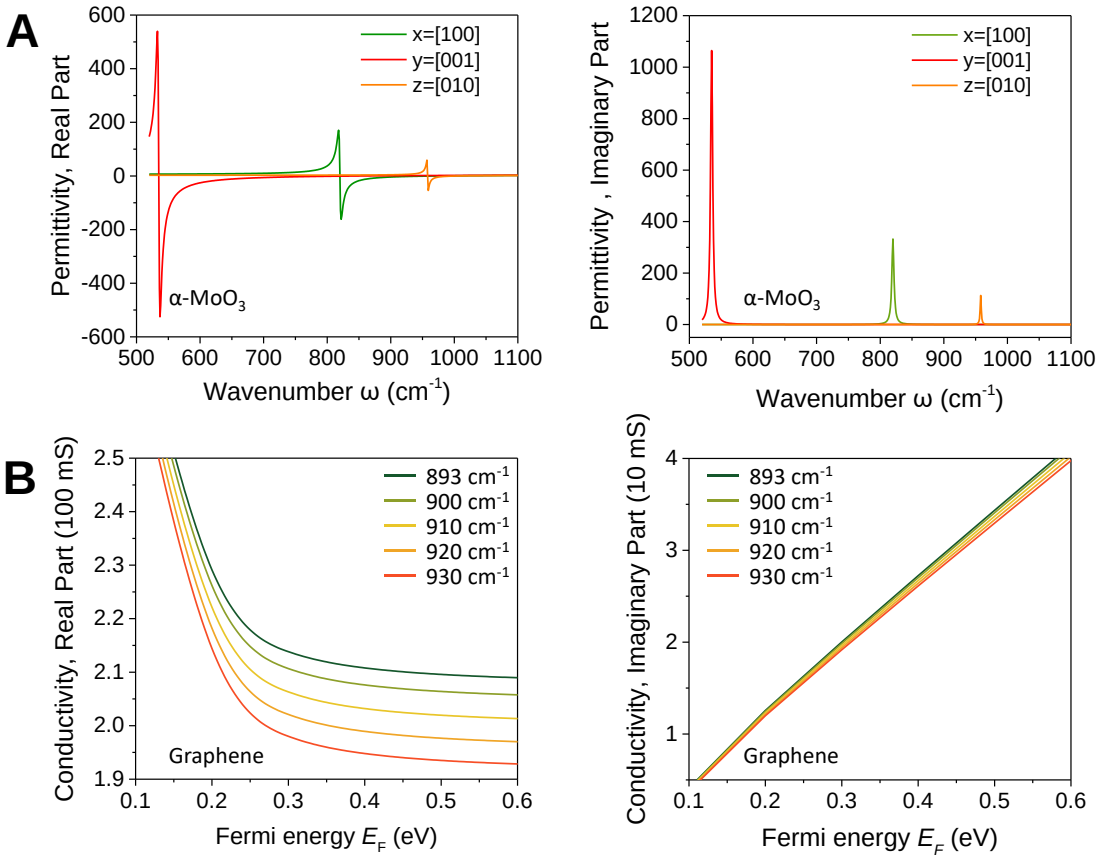

Fig. S1. Optical parameters of graphene and α-MoO_3. (A) Real (left) and imaginary part (right) of the permittivity of α-MoO_3 along different principal directions. The permittivity is obtained by fitting the obtained data with a Lorentzian model. (**B**) Real (left) and imaginary part (right) of the conductivity of graphene as a function of Fermi energy and frequency, following Eq. (*S*1).

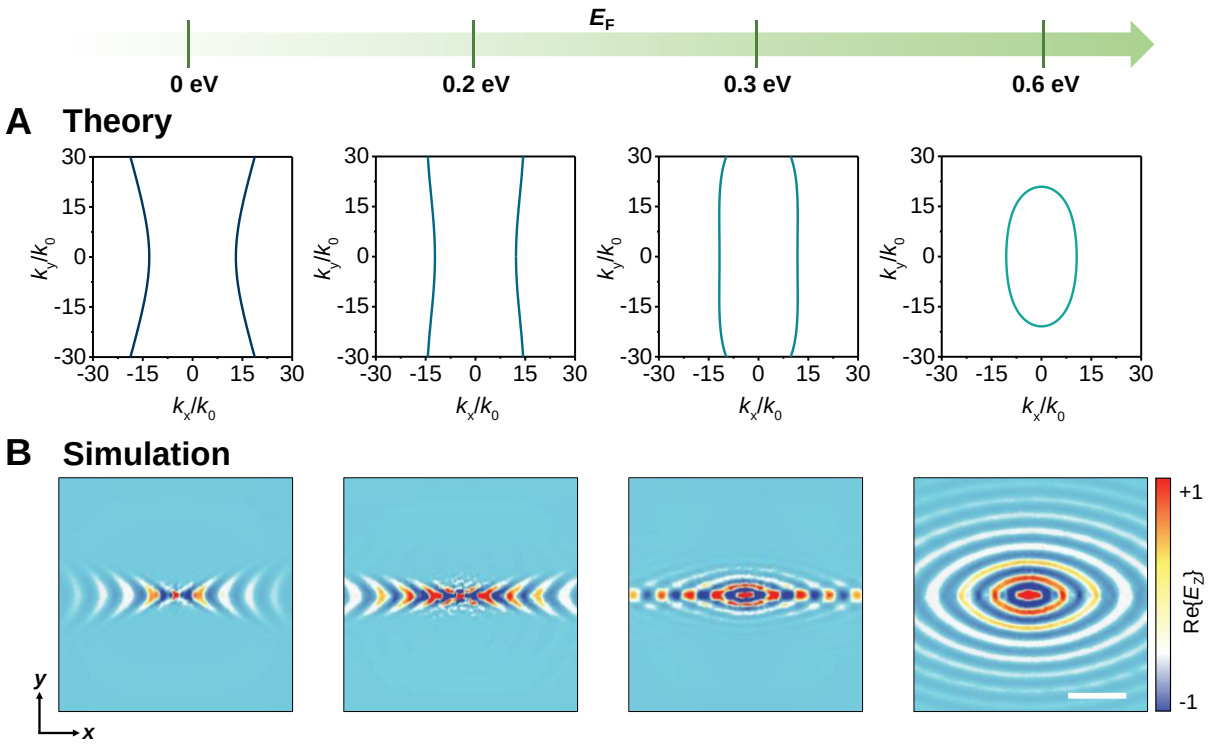

Fig. S2. Hybrid polaritons in a graphene/α-MoO_3 heterostructure. (**A**) Theoretically calculated IFCs of hybrid polaritons with various graphene Fermi energies of E_F = 0 eV, 0.2 eV, 0.3 eV, and 0.6 eV, respectively. (**B**) Numerically simulated electric field distribution of hybrid polaritons corresponding to panel (A). The thickness of α-MoO_3 is set at 240 nm. The illumination frequency is fixed at 893 cm^{-1}. The scale bar indicates 2 μm.

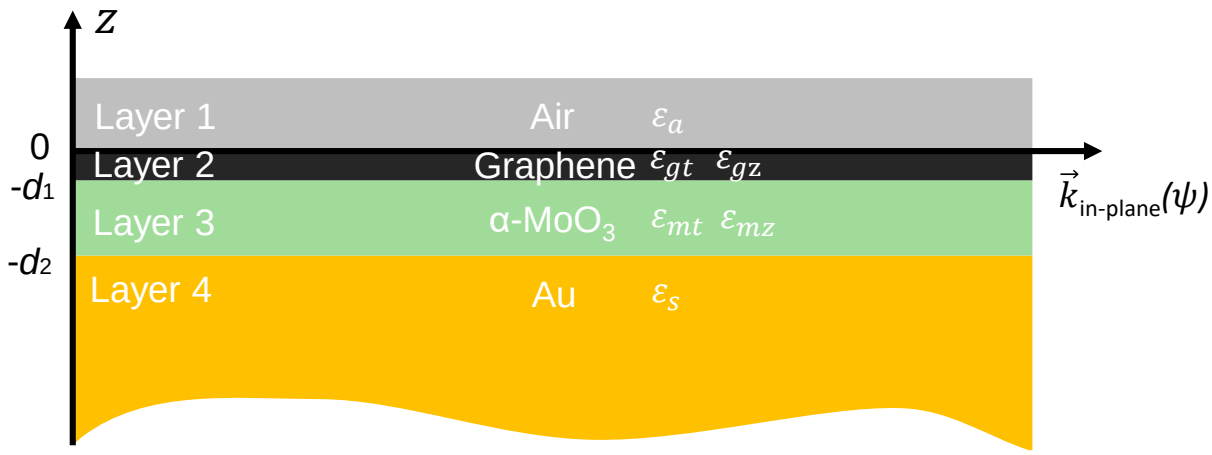

Fig. S3. Illustration of the device structure used in our theoretical model. Layers 1 to 4 correspond to air, graphene, α-MoO_3, and Au, respectively. Each layer is described by its dielectric tensor.

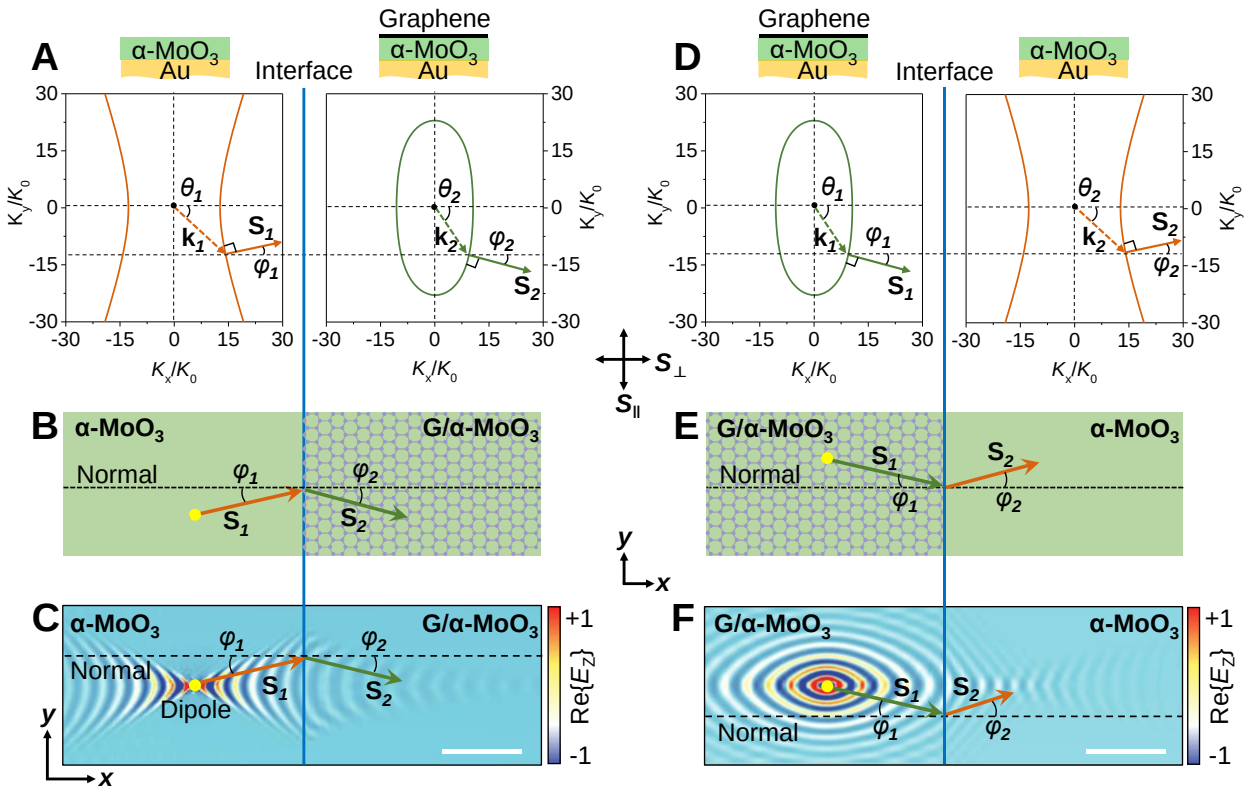

Fig. S4. Illustration of reversible polariton negative refraction. (**A, D**) Isofrequency contours of hyperbolic polaritons in α-MoO_3 and hybrid polaritons in graphene/α-MoO_3. The upper illustration shows a cross-section of each structure. Negative refraction of polaritons takes place at the interface between the two sides of the graphene edge due to the conservation of tangential wave vector components. (**B, E**) Schematic diagram of the typical Poynting vectors relative to the normal to interface on both sides in the *x*-*y* plane. Negative refraction results in the Poynting vectors of the incident and transmitted polaritons on the same side of the interface normal. (**C, F**) Numerically simulated field distributions (real part of the out-of-plane component of the electric field, Re{*Ez*}) illustrating negative refraction and planar focusing. A source dipole (yellow dot) is placed 100 nm above the surface to launch the polaritons. The α-MoO_3 thickness is 242 nm, the graphene Fermi energy is 0.5 eV, and the illumination frequency is 893 cm^{-1}. The scale bar indicates 2 μm. For the refraction angle, we specify "+" on the upside of the interface normal and "-" on the downside.

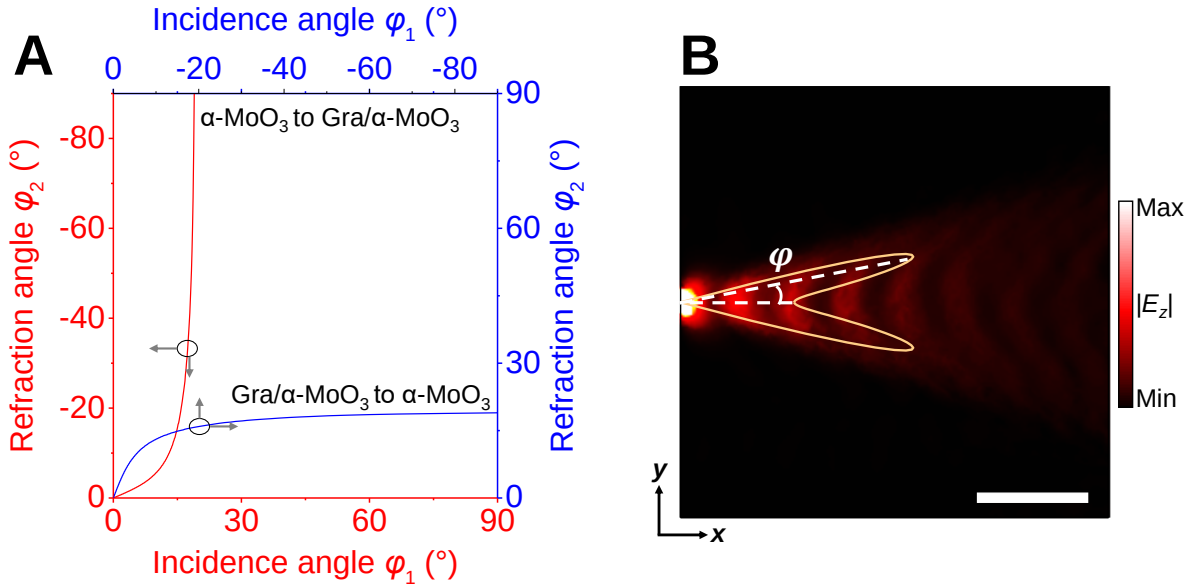

Fig. S5. Theoretical analysis of the incidence and refraction angles. (A) Incidence angle φ_1 as a function of refraction angle φ_2 for negative refraction after transmission through the in-plane interface for the two reversed cases (see labels). These angles refer to the incidence and refracted polariton Poynting vector **S**. **(B)** Numerical simulation of the electric field $|E_z|$ (color plot) excited by a point electric dipole placed 100 nm above the α-MoO_3 film, together with the polar distribution of the electric field in real space (orange solid curve). φ indicates the incidence angle of the polariton Poynting vector. The scale bar indicates 1 μm.

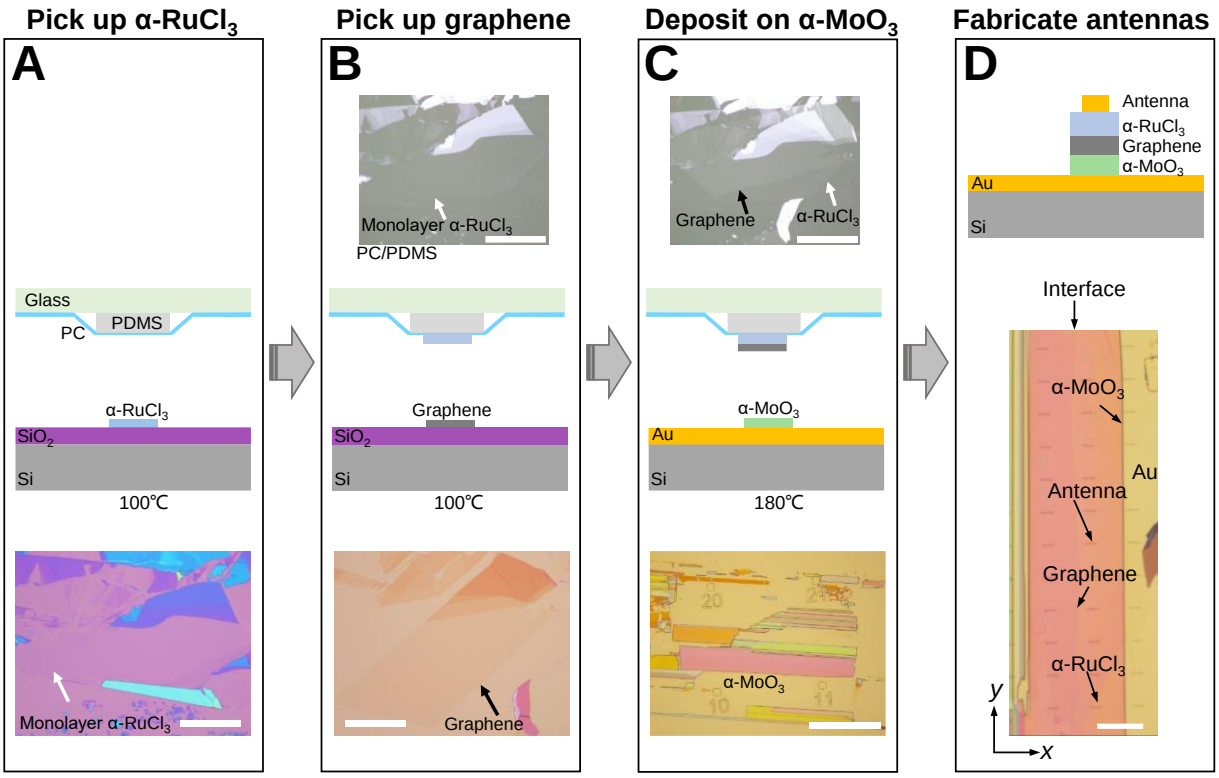

Fig. S6. Illustration of the dry transfer process. (A) A glass/PDMS/PC stamp is brought into contact with a monolayer of α-$RuCl_3$ exfoliated on a SiO_2 (300 nm)/Si substrate at 100℃ and then withdrawn. **(B)** The stamp along with α-$RuCl_3$ is contracted with an exfoliated graphene monolayer at 100 ℃, and again slowly withdrawn. **(C, D)** The α-$RuCl_3$/graphene is aligned and contracted with an α-MoO_3 film previously exfoliated on a Au (60 nm)/Si substrate. Then, the temperature is raised to 180 ℃ and the stack is released onto the α-MoO_3 film, forming an α-$RuCl_3$/graphene/α-MoO_3 heterostructure. Scale bars indicate 20 μm in panels (A-C) and 8 μm in panel (D).

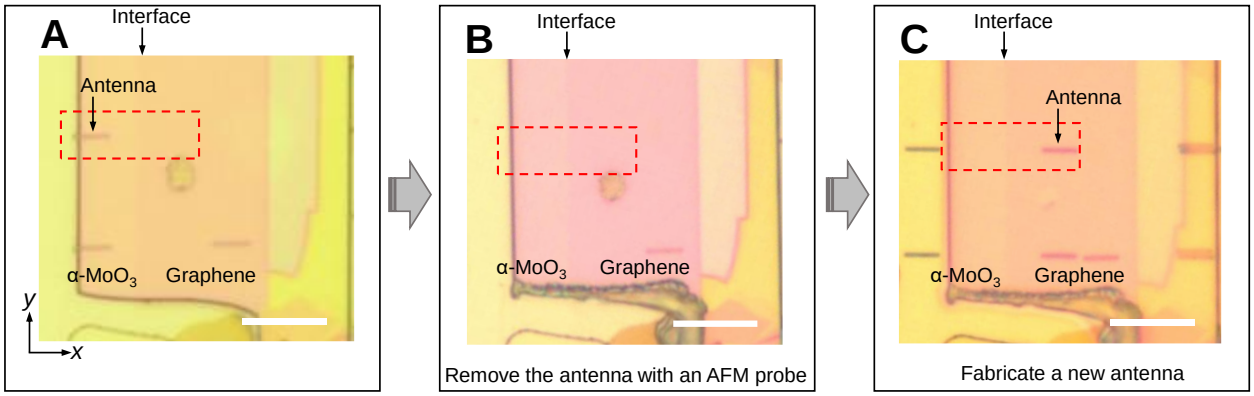

Fig. S7. Illustration of AFM probe transfer method. (A) Gold antenna arrays on the α-MoO_3 film. **(B)** The gold antennas on α-MoO_3 are removed away by an AFM tip. **(C)** Another gold antenna array is fabricated on the graphene/α-MoO_3 side. This sample is used for near-field measurements in Fig. 2 in the main text. Scale bars indicate 8 μm.

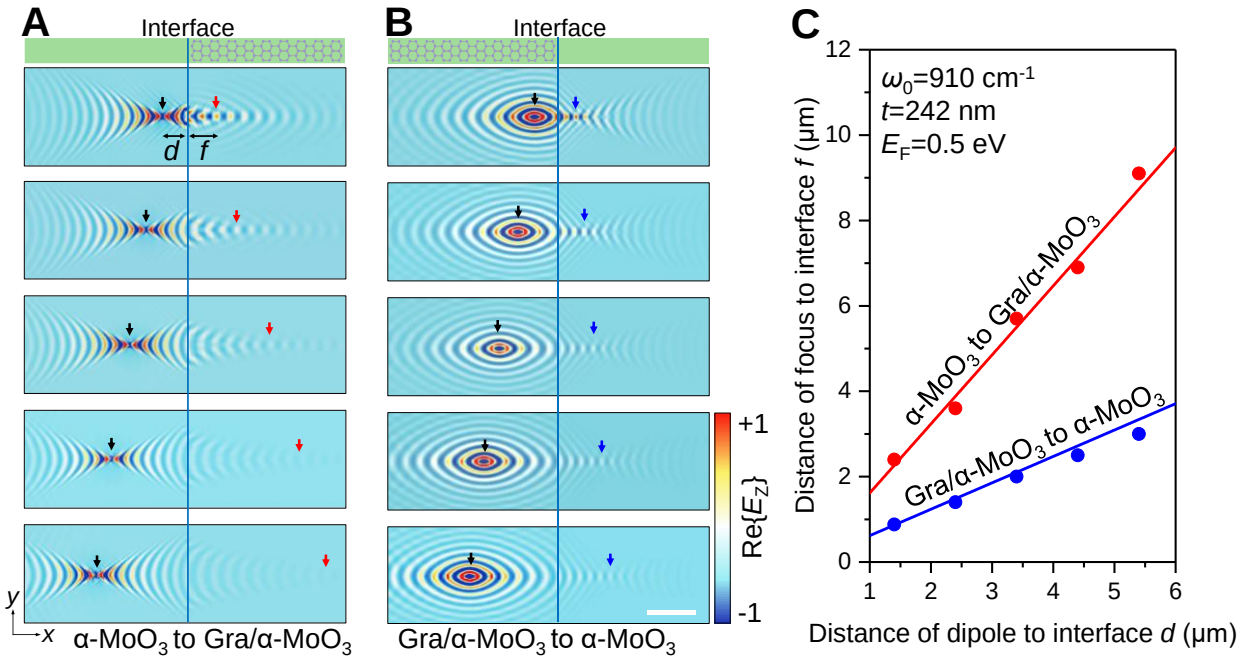

Fig. S8. Simulation and theoretical analysis of the spatial relationship between focal and launching source position. (A) Simulated spatial distribution of the electric field Re{E_z} showing negative refraction from α-MoO_3 with a hyperbolic wave to graphene/α-MoO_3 with an elliptic wave. d and f represent the distance of the interface to the launching source and focal spot positions, respectively. The black arrows indicate the position of the emitting dipole. The red and blue arrows mark the focal spot. **(B)** Reversible negative refraction relative to panel (A), where the dipole is moved to the graphene/α-MoO_3 side. The scale bar indicates 2 μm. **(C)** d as a function of f for the configurations in panels (A) (red) and (B) (blue). The dots are extracted from the simulations presented in panels (A, B), while the solid lines stand for the theoretical analysis based on the method described in Note S3.

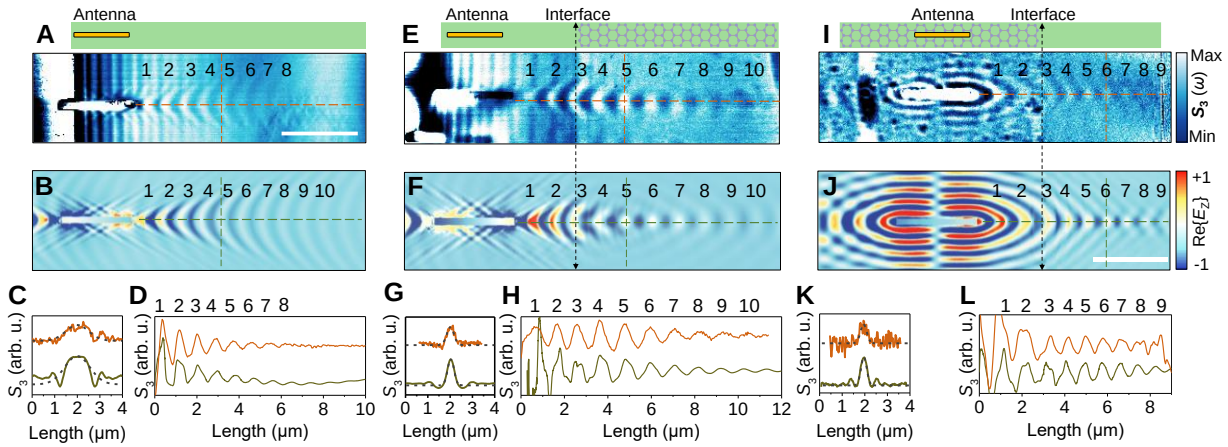

Fig. S9. Experimentally measured near-field distributions of polaritons and corresponding simulated field distributions Re{E_z}. (A-D) Hyperbolic polaritons launched and propagated in bare α-MoO_3 as a control experiment. **(E-H)** Hyperbolic polaritons launched from α-MoO_3 to the interface, undergoing negative refraction and focusing. **(I-L)** Reversed negative refraction relative to panels (E-H), where the antenna is now placed on the graphene/α-MoO_3 side. **(A, E, I)** Experimentally measured near-field amplitude of polaritons. **(B, F, J)** Simulated field amplitude Re{E_z} corresponding to panels (A, E, I). **(C, G, K)** Near-field profiles of the signal along the orange and green vertical dashed lines in panels (A, B), (E, F), and (I, J), respectively. The black dashed curves are fitting Gaussians. **(D, H, L)** Near-field profiles of the signal along the orange and green horizontal dashed lines in panels (A, B), (E, F), and (I, J), respectively. All the experimental results are measured from the in-situ sample shown in Fig. 2 and fig. S7. The thickness of α-MoO_3 is 242 nm. The scale bar indicates 3 μm. The graphene is prepared by mechanical exfoliation and statically doped to a Fermi energy E_F = 0.5 eV by a monolayer of α-$RuCl_3$. The illumination frequency is fixed at ω_0 = 893 cm^{-1}.

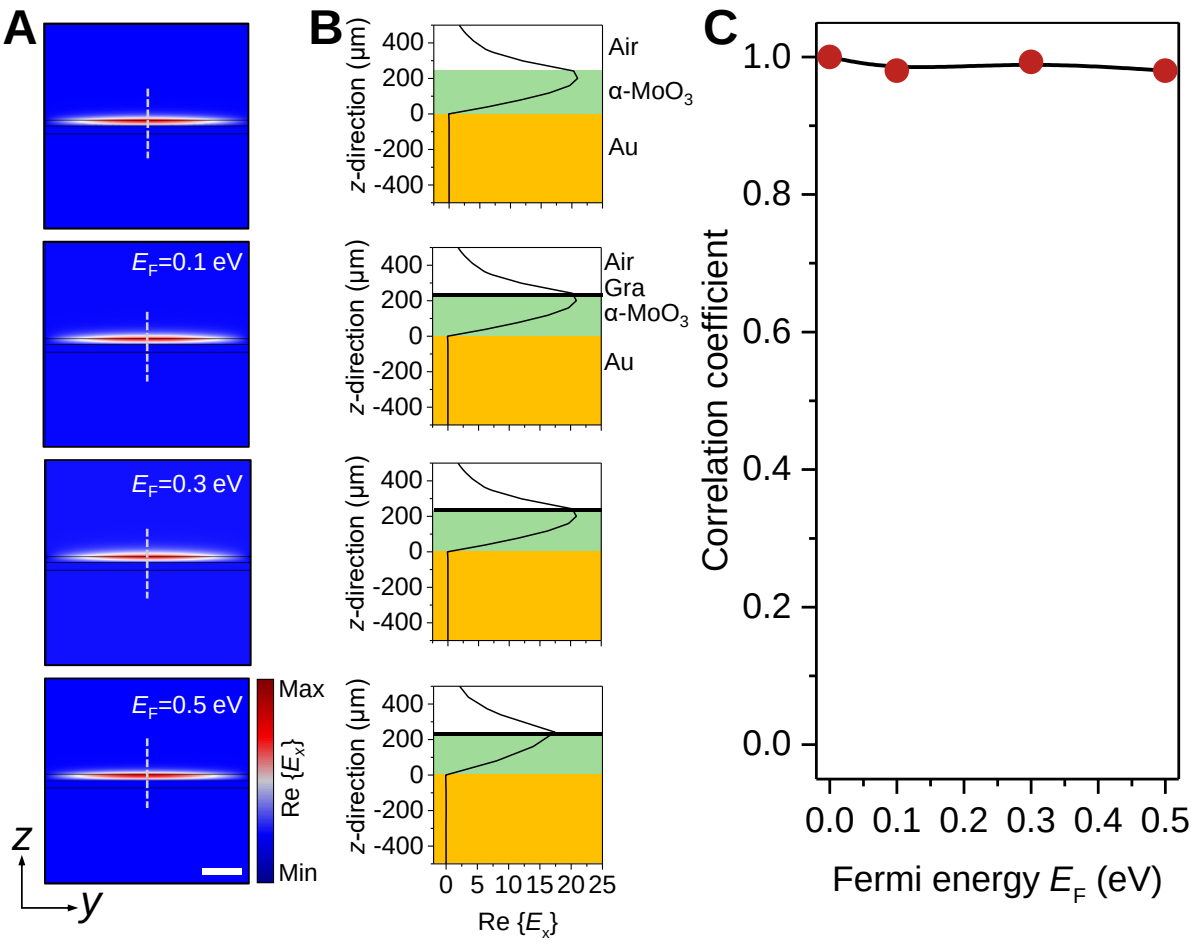

Fig. S10. Simulation of modal-profile matching. (A) Mode profiles for different graphene Fermi energies. The thickness of α-MoO_3 is 242 nm. The scale bar indicates 3 μm. The illumination frequency is fixed at ω_0=900 cm^{-1}. **(B)** Electric field profiles for different graphene Fermi energies corresponding to panel (A). **(C)** Correlation coefficient of the electric field profiles for different graphene Fermi energies compared with that of bare α-MoO_3, shown at the top of panel (B). The modal-profile mismatch is less than 3% at different graphene Fermi energies due to the strong overlap of the surface modes on both sides.

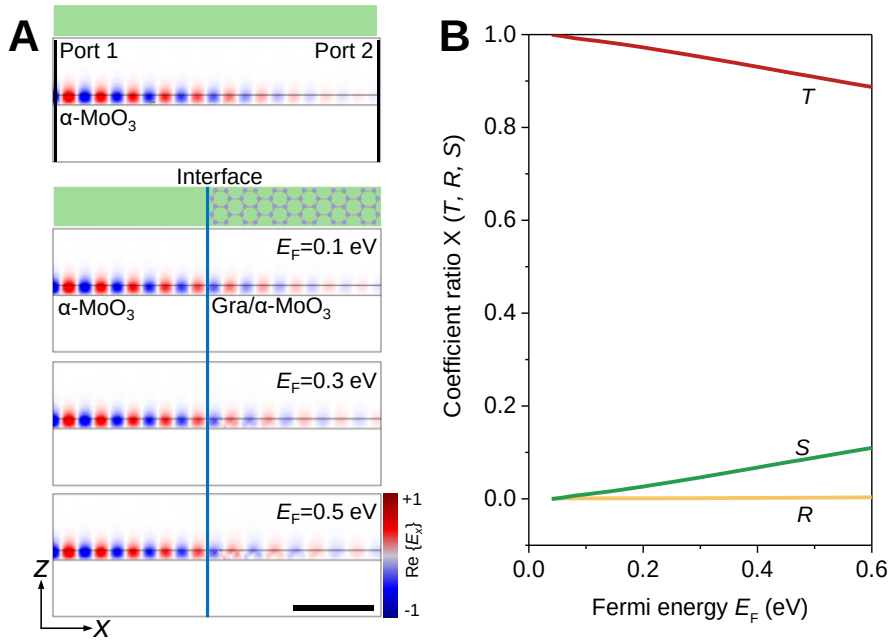

Fig. S11. Analysis of optical losses at the graphene interface. (A) Simulated spatial distribution of the electric field along the *x* direction as polaritons propagate from α-MoO_3 to graphene/α-MoO_3 for different graphene Fermi energies (see labels). Since this is a port excitation, we only consider the polaritons of normal incidence. The thickness of α-MoO_3 is 242 nm. The scale bar indicates 2 μm. The illumination frequency is fixed at ω_0 = 900 cm^{-1}. **(B)** Polaritonic reflectance (yellow), transmittance (red), and scattering (green) as a function of graphene Fermi energy. Thanks to the single-atom thickness of graphene, losses stemming from scattering at the interface are expected to be negligible and, although they increase with the graphene Fermi energy, the overall loss does not exceed 12%.

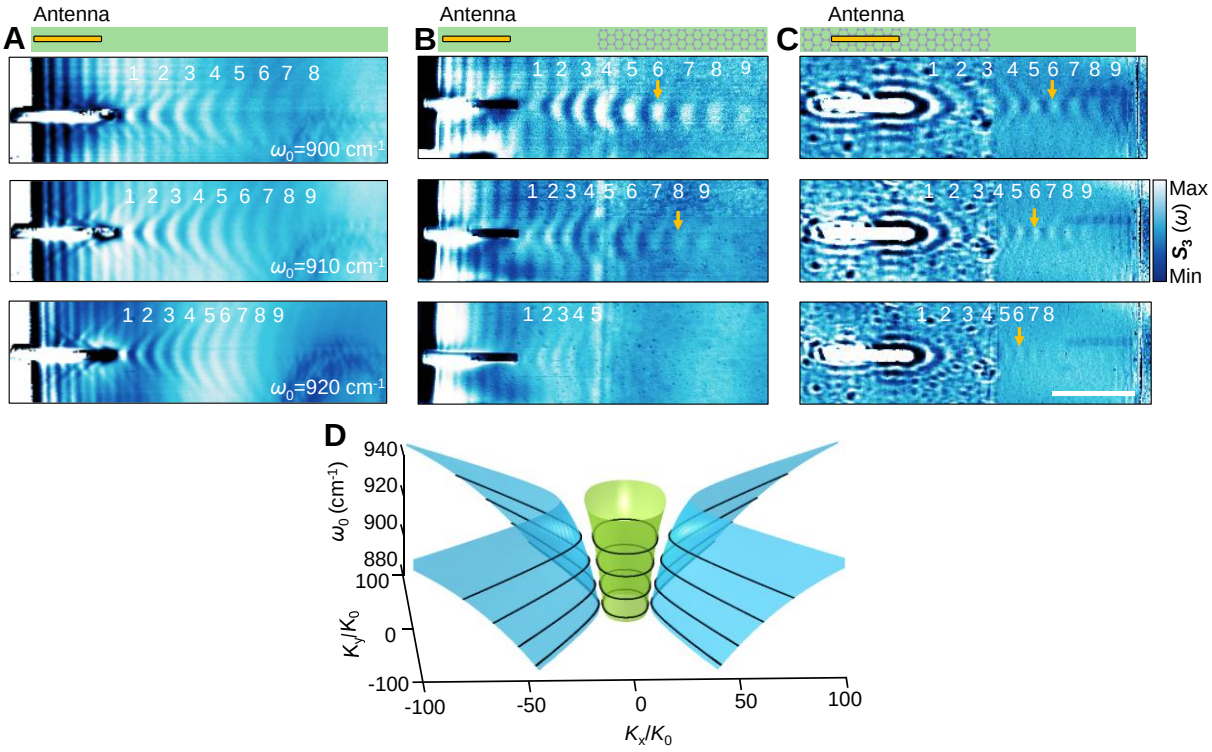

Fig. S12. Wide angle negative refraction over a broad spectral range. (A) Hyperbolic polaritons launched and propagated in natural α-MoO_3 as a control experiment. (**B**) Measured near-field images showing negative refraction from α-MoO_3 to graphene/α-MoO_3 with illumination frequencies ranging from 900 to 920 cm^{-1} (see labels). (**C**) Negative refraction from graphene/α-MoO_3 to α-MoO_3. All experimental results are measured from the same in-situ sample as in Fig. 2. The scale bar indicates 3 μm. (**D**) Three-dimensional representation of the polariton IFCs in α-MoO_3 (blue) and graphene/α-MoO_3 heterostructure (green), with experimentally measured frequencies represented by black curves. The opening angle β of PhPs in α-MoO_3 increases with the illumination frequency, which weakens the focusing effect produced by negative refraction from α-MoO_3 to graphene/α-MoO_3 because of the increased spatial incidence range of PhPs in α-MoO_3. On the contrary, focusing should be enhanced with an increase of frequency for negative refraction from graphene/α-MoO_3 to α-MoO_3 due to the increase in refraction angle, which is related to the opening angle.

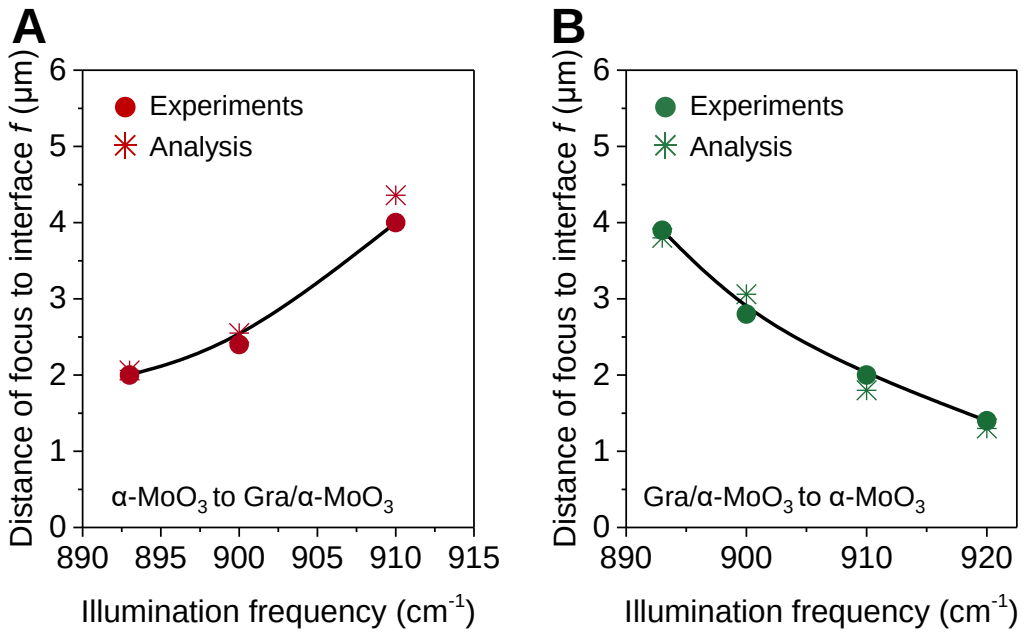

Fig. S13. Experimental relationship between focal position and various illumination frequencies. (A, B) Focal distance from the interface as a function of illumination frequency. The red and green dots are extracted from experimental results in Fig. 2 and fig. S12, while crosses represent theoretical results obtained by using the method described in Note S3, and the solid curves are guides to the eyes.

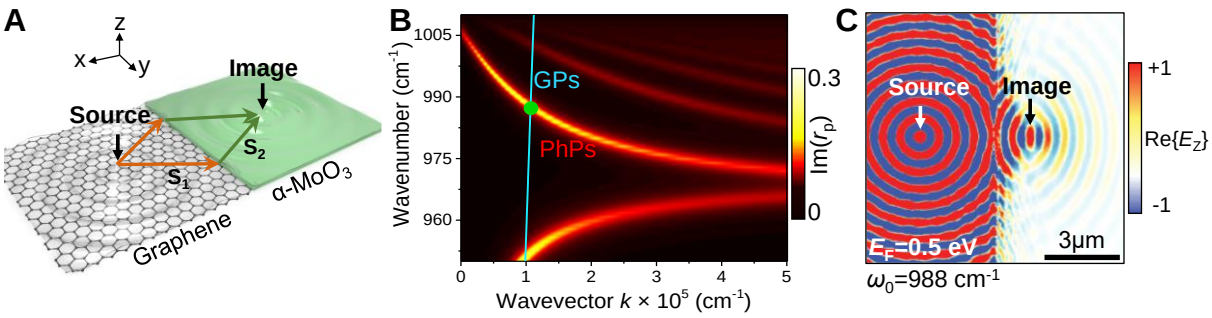

Fig. S14. Negative refraction by negative group velocity of reversed dispersion. (**A**) Schematic of negative refraction between plasmons in graphene and phonon polaritons in α-MoO_3 using an in-plane heterostructure. $\mathbf{S}_1$ and $\mathbf{S}_2$ indicate the Poynting vectors of plasmon and phonon polaritons, respectively. (**B**) Dispersion of graphene plasmons and phonon polaritons in α-MoO_3, corresponding to the left and right region in the panel (A), respectively. (**C**) Simulated spatial distribution of the electric field Re{E_z} launched by a dipole source at a frequency of 988 cm^{-1} (corresponding to the intersection of the green dot in panel (B)), showing negative refraction. The Fermi energy of graphene is set to 0.5 eV and the thickness of α-MoO_3 is 260 nm.

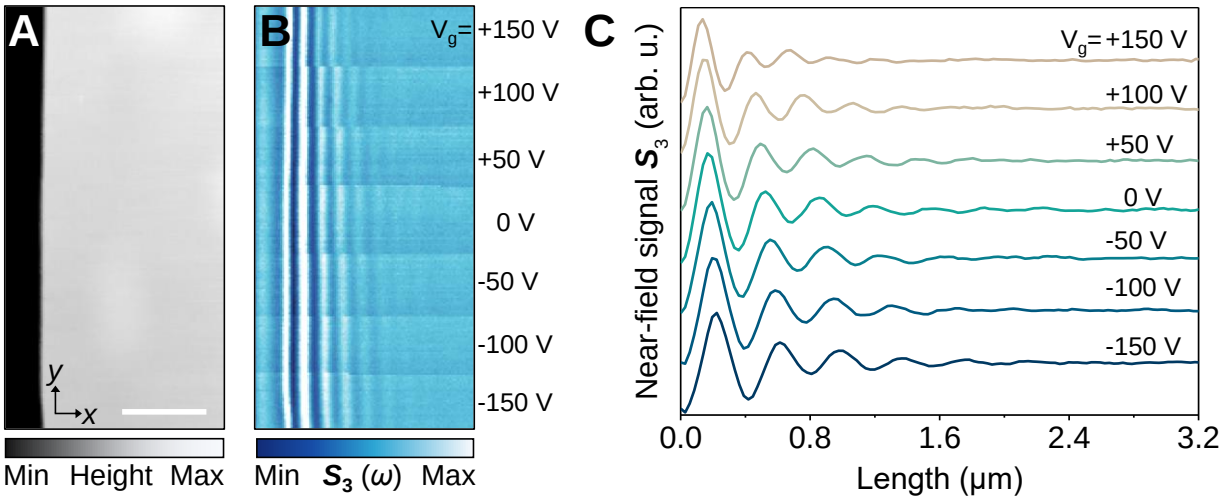

524

525 **Fig. S15. Gate-tunable hybrid polaritons.** (**A**) Topography images of the α-MoO_3 edge
526 corresponding to the samples in Fig. 3. The scale bar indicates 1.5 μm. (**B**) Real-space infrared
527 nano-images of gate-tunable hybrid polaritons along the x direction (crystal axis [100] of α-MoO_3).
528 (**C**) Near-field profiles extracted from panel (B). The α-MoO_3 thickness is 60 nm and the
529 illumination frequency is 893 cm^{-1}.

530

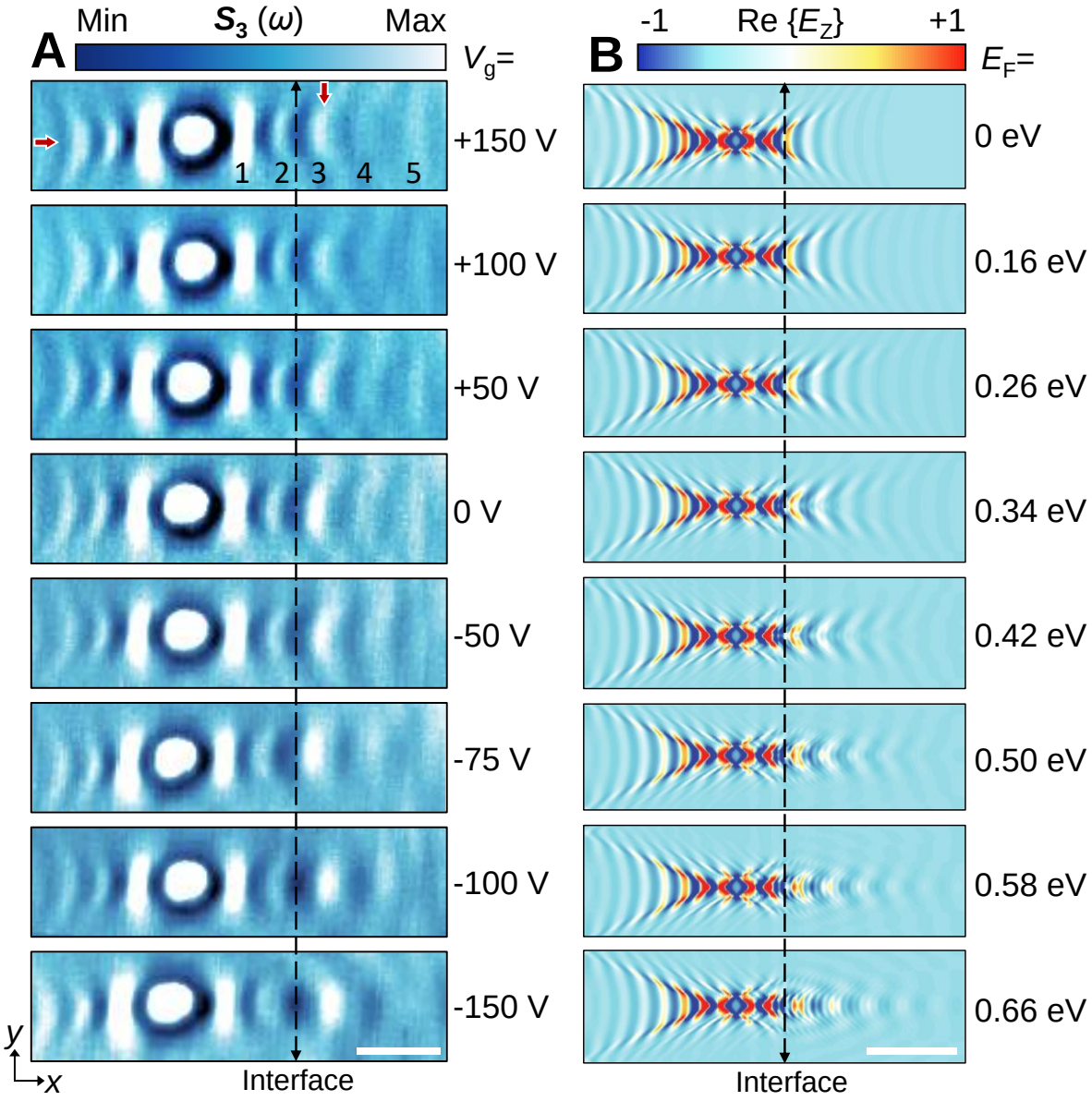

Fig. S16. Gate-tunable negative refraction with different graphene Fermi energies. (A) Experimental near-field images showing gate tunning of negative refraction from α-MoO_3 to graphene/α-MoO_3 with voltages arranged from +150 to -150 V. The scale bar indicates 1.5 μm. **(B)** Numerically simulated negative refraction with various Fermi energies of graphene from E_F=0 to 0.66 eV, corresponding to the experimental gate voltages. The experimentally recorded polaritons are represented by interference fringes excited by the tip and reflected by the hole edge. The polaritons are excited by the incident light directly on the hole edge in the simulation. Therefore, there is a two-fold spatial relationship between these two results. The scale bar indicates 0.5 μm (A) and 2.5 μm (B), respectively. The α-MoO_3 thickness is 60 nm and the illumination frequency is 893 cm^{-1} in all panels.

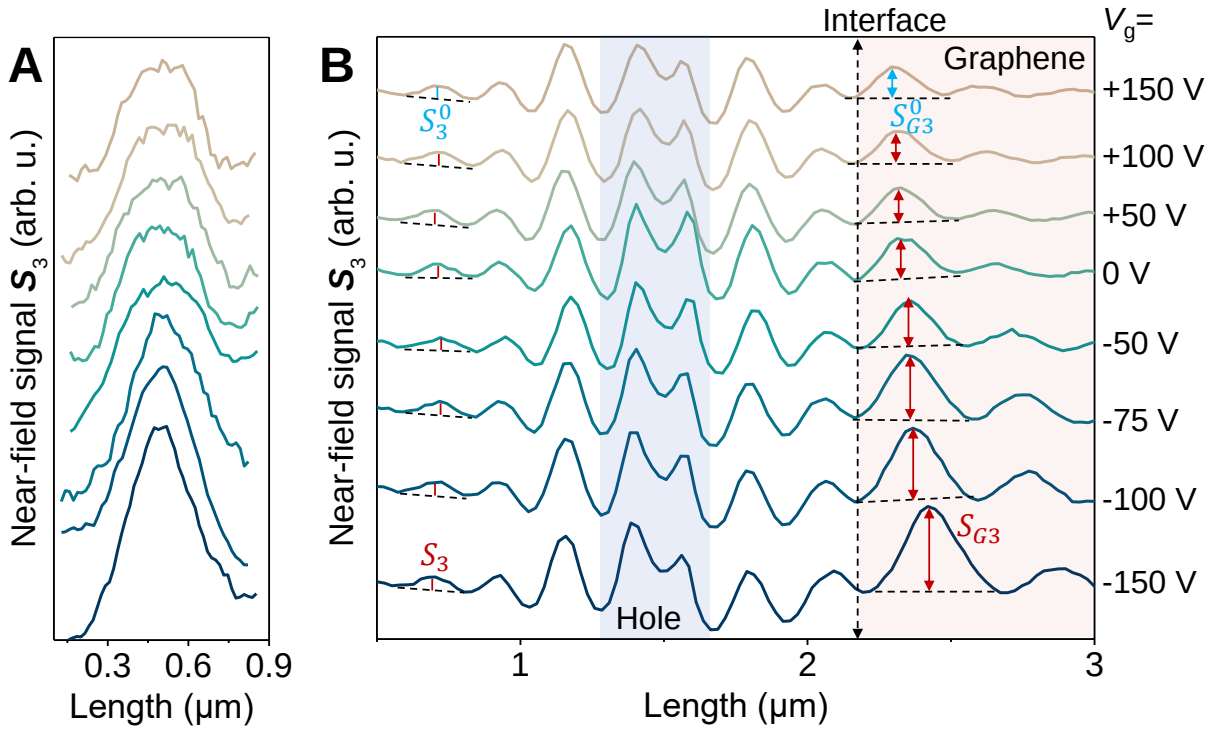

Fig. S17. Extraction analysis of FWHM and intensity enhancement of the focal spots for various gate voltages. FWHM and intensity enhancement are extracted along the *y* and *x* directions (vertical (the third fringe) and horizontal red arrows in fig. S16, respectively). The FWHM can be obtained by fitting the near-field signal profiles in panel (A). The intensity enhancement can be determined by comparing the intensity ratio of the focusing fringe to the same order fringe without a negative refraction effect (*i.e.* $[(S_{G3}/S_3)/(S_{G3}^0/S_3^0)]^2$), where S_{G3}^0/S_3^0 represents the effects from the surface conductance of graphene and it is subtracted to obtain the field enhancement caused only by the focusing of negative refraction.

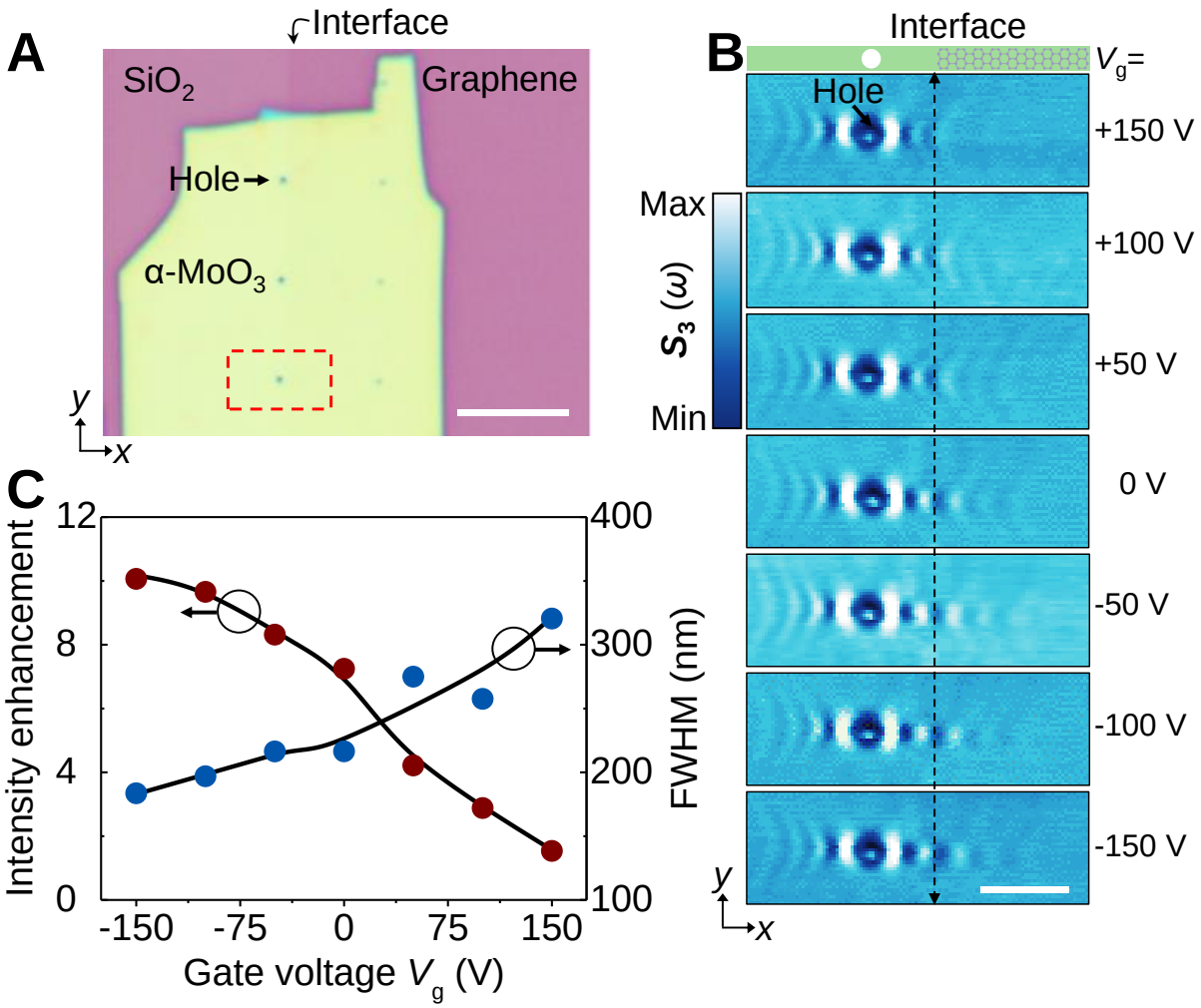

Fig. S18. Gate-tunable negative refraction of another sample. (**A**) Optical image of a gate-tunable device consisting of (from top to bottom) an α-MoO_3 film, monolayer graphene, and SiO_2 substrate. The black horizontal arrow indicates the position of the fabricated circular holes with a diameter of 400 nm. The scale bar stands for 10 μm. (**B**) Experimentally measured near-field images of gate-tunable negative refraction from hyperbolic α-MoO_3 to elliptic graphene/α-MoO_3 with bias voltages varying from +150 V to -150 V. The focal point yields FWHM as small as 185 nm at V_g=-150 V (*i.e.*, ~1/60 or 1.6% of the free-space light wavelength). The vertical black dashed line represents the graphene edge. The α-MoO_3 thickness is d = 50 nm. The illumination frequency is fixed at 893 cm^{-1}. The scale bar indicates 2 μm. (**C**) Intensity enhancement and FWHM of the focal spots for various gate voltages, taken from the experimental measurements in panel (B).

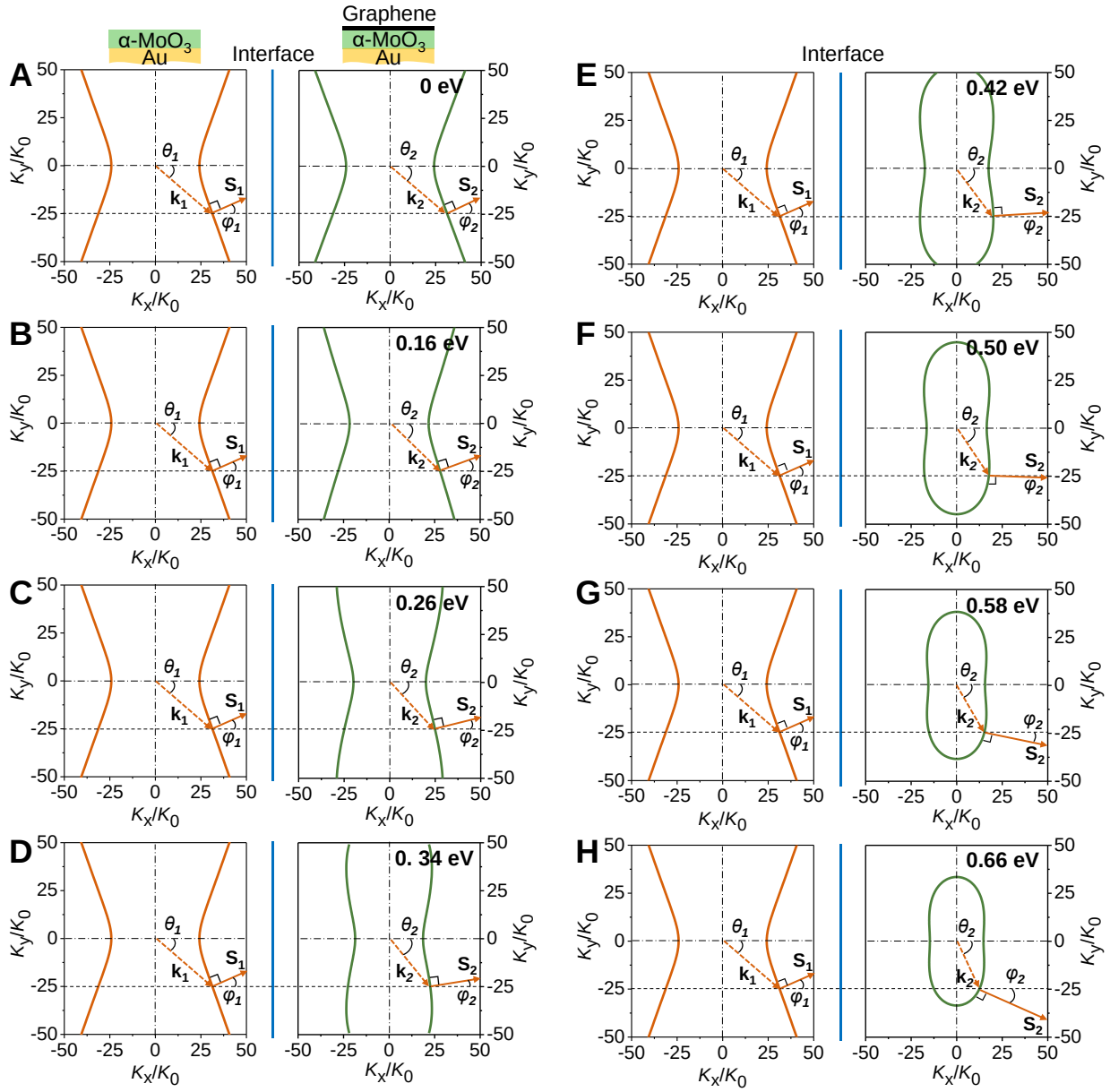

Fig. S19. IFC analysis of the transition from normal to negative refraction by gate-tuning. Normal refraction occurs for E_F = 0 eV, 0.16 eV, 0.26 eV, 0.34 eV, and 0.42 eV; "zero" refraction takes place at a Fermi energy about E_F = 0.50 eV; negative refraction is observed for Fermi energies E_F = 0.58 eV and 0.66 eV. These Fermi energies correspond in turn to experimental gate voltages V_g = +150 V, +100 V, +50 V, 0 V, -50 V, -75 V, -100 V, and -150 V, respectively. The α-MoO_3 thickness is 60 nm and the illumination frequency is 893 cm^{-1}. For the angle of refraction, we specify "+" on the upside of the interface normal and "-" on the downside.

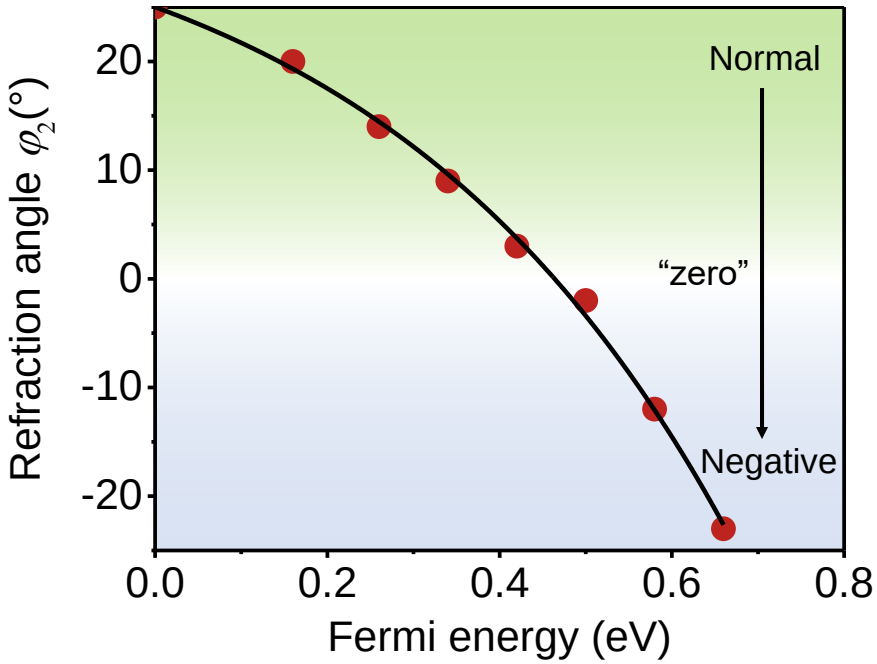

Fig. S20. Refraction angle φ_2 as a function of gate-tuning graphene Fermi energy. The green and blue shaded areas indicate the transition from normal to negative refraction. The red dots are extracted from fig. S19 and the black curve is a guide to the eyes.

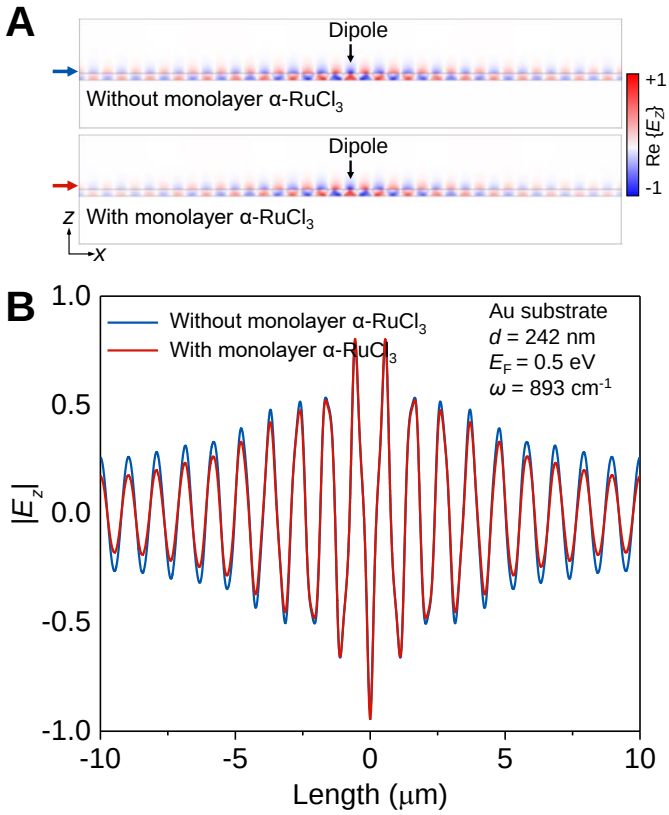

Fig. S21. Effect of monolayer α-$RuCl_3$ on the propagation of hybrid polaritons. (A) Numerically simulated field distribution of hybrid plasmon-phonon polaritons in graphene/α-MoO_3 with and without monolayer α-$RuCl_3$. **(B)** Near-field profiles taken at the positions marked by blue and red horizontal arrows in panel (A). The value of $|E_z|$ is normalized to the maximum electric-field intensity. The Fermi energy of graphene is set to E_F = 0.5 eV. The α-MoO_3 thickness is 242 nm. The illumination frequency is 893 cm^{-1}.

References and Notes

1. J. B. Pendry, Negative refraction makes a perfect lens. *Phys. Rev. Lett.* **85**, 3966–3969 (2000). doi:10.1103/PhysRevLett.85.3966 Medline

2. R. A. Shelby, D. R. Smith, S. Schultz, Experimental verification of a negative index of refraction. *Science* **292**, 77–79 (2001). doi:10.1126/science.1058847 Medline

3. J. Yao, Z. Liu, Y. Liu, Y. Wang, C. Sun, G. Bartal, A. M. Stacy, X. Zhang, Optical negative refraction in bulk metamaterials of nanowires. *Science* **321**, 930 (2008). doi:10.1126/science.1157566 Medline

4. G.-H. Lee, G.-H. Park, H.-J. Lee, Observation of negative refraction of Dirac fermions in graphene. *Nat. Phys.* **11**, 925–929 (2015). doi:10.1038/nphys3460

5. H. He, C. Qiu, L. Ye, X. Cai, X. Fan, M. Ke, F. Zhang, Z. Liu, Topological negative refraction of surface acoustic waves in a Weyl phononic crystal. *Nature* **560**, 61–64 (2018). doi:10.1038/s41586-018-0367-9 Medline

6. A. Pimenov, A. Loidl, P. Przyslupski, B. Dabrowski, Negative refraction in ferromagnet-superconductor superlattices. *Phys. Rev. Lett.* **95**, 247009 (2005). doi:10.1103/PhysRevLett.95.247009 Medline

7. W. Cai, U. K. Chettiar, A. V. Kildishev, V. M. Shalaev, Optical cloaking with metamaterials. *Nat. Photonics* **1**, 224–227 (2007). doi:10.1038/nphoton.2007.28

8. D. R. Smith, J. B. Pendry, M. C. Wiltshire, Metamaterials and negative refractive index. *Science* **305**, 788–792 (2004). doi:10.1126/science.1096796 Medline

9. K. L. Tsakmakidis, A. D. Boardman, O. Hess, 'Trapped rainbow' storage of light in metamaterials. *Nature* **450**, 397–401 (2007). doi:10.1038/nature06285 Medline

10. E. Cubukcu, K. Aydin, E. Ozbay, S. Foteinopoulou, C. M. Soukoulis, Negative refraction by photonic crystals. *Nature* **423**, 604–605 (2003). doi:10.1038/423604b Medline

11. P. V. Parimi, W. T. Lu, P. Vodo, S. Sridhar, Photonic crystals: Imaging by flat lens using negative refraction. *Nature* **426**, 404 (2003). doi:10.1038/426404a Medline

12. A. Poddubny, I. Iorsh, P. Belov, Y. Kivshar, Hyperbolic metamaterials. *Nat. Photonics* **7**, 948–957 (2013). doi:10.1038/nphoton.2013.243

13. J. S. Gomez-Diaz, A. Alù, Flatland optics with hyperbolic metasurfaces. *ACS Photonics* **3**, 2211–2224 (2016). doi:10.1021/acsphotonics.6b00645

14. Q. Chen, Y. Yang, L. Zhang, J. Chen, M. Li, X. Lin, R. Li, Z. Wang, B. Zhang, H. Chen, Negative refraction of ultra-squeezed in-plane hyperbolic designer polaritons. *Photon. Res.* **9**, 1540–1549 (2021). doi:10.1364/PRJ.424739

15. T. Xu, A. Agrawal, M. Abashin, K. J. Chau, H. J. Lezec, All-angle negative refraction and active flat lensing of ultraviolet light. *Nature* **497**, 470–474 (2013). doi:10.1038/nature12158 Medline

16. H. J. Lezec, J. A. Dionne, H. A. Atwater, Negative refraction at visible frequencies. *Science* **316**, 430–432 (2007). doi:10.1126/science.1139266 Medline

17. V. Podolskiy, A. Sarychev, V. Shalaev, Plasmon modes and negative refraction in metal nanowire composites. *Opt. Express* **11**, 735–745 (2003). doi:10.1364/OE.11.000735 Medline

18. A. Vakil, N. Engheta, Transformation optics using graphene. *Science* **332**, 1291–1294 (2011). doi:10.1126/science.1202691 Medline

19. D. N. Basov, M. M. Fogler, F. J. García de Abajo, Polaritons in van der Waals materials. *Science* **354**, aag1992 (2016). doi:10.1126/science.aag1992 Medline

20. T. Low, A. Chaves, J. D. Caldwell, A. Kumar, N. X. Fang, P. Avouris, T. F. Heinz, F. Guinea, L. Martin-Moreno, F. Koppens, Polaritons in layered two-dimensional materials. *Nat. Mater.* **16**, 182–194 (2017). doi:10.1038/nmat4792 Medline

21. Q. Zhang, G. Hu, W. Ma, P. Li, A. Krasnok, R. Hillenbrand, A. Alù, C.-W. Qiu, Interface nano-optics with van der Waals polaritons. *Nature* **597**, 187–195 (2021). doi:10.1038/s41586-021-03581-5 Medline

22. Y. Wu, J. Duan, W. Ma, Q. Ou, P. Li, P. Alonso-González, J. D. Caldwell, Q. Bao, Manipulating polaritons at the extreme scale in van der Waals materials. *Nat. Rev. Phys.* **4**, 578–594 (2022). doi:10.1038/s42254-022-00472-0

23. K. V. Sreekanth, A. De Luca, G. Strangi, Negative refraction in graphene-based hyperbolic metamaterials. *Appl. Phys. Lett.* **103**, 023107 (2013). doi:10.1063/1.4813477

24. X. Lin, Y. Yang, N. Rivera, J. J. López, Y. Shen, I. Kaminer, H. Chen, B. Zhang, J. D. Joannopoulos, M. Soljačić, All-angle negative refraction of highly squeezed plasmon and phonon polaritons in graphene-boron nitride heterostructures. *Proc. Natl. Acad. Sci. U.S.A.* **114**, 6717–6721 (2017). doi:10.1073/pnas.1701830114 Medline

25. W. Ma, P. Alonso-González, S. Li, A. Y. Nikitin, J. Yuan, J. Martín-Sánchez, J. Taboada-Gutiérrez, I. Amenabar, P. Li, S. Vélez, C. Tollan, Z. Dai, Y. Zhang, S. Sriram, K. Kalantar-Zadeh, S.-T. Lee, R. Hillenbrand, Q. Bao, In-plane anisotropic and ultra-low-loss polaritons in a natural van der Waals crystal. *Nature* **562**, 557–562 (2018). doi:10.1038/s41586-018-0618-9 Medline

26. Z. Zheng, N. Xu, S. L. Oscurato, M. Tamagnone, F. Sun, Y. Jiang, Y. Ke, J. Chen, W. Huang, W. L. Wilson, A. Ambrosio, S. Deng, H. Chen, A mid-infrared biaxial hyperbolic van der Waals crystal. *Sci. Adv.* **5**, eaav8690 (2019). doi:10.1126/sciadv.aav8690 Medline

27. G. Hu, Q. Ou, G. Si, Y. Wu, J. Wu, Z. Dai, A. Krasnok, Y. Mazor, Q. Zhang, Q. Bao, C.-W. Qiu, A. Alù, Topological polaritons and photonic magic angles in twisted α-MoO_3 bilayers. *Nature* **582**, 209–213 (2020). doi:10.1038/s41586-020-2359-9 Medline

28. M. Chen, X. Lin, T. H. Dinh, Z. Zheng, J. Shen, Q. Ma, H. Chen, P. Jarillo-Herrero, S. Dai, Configurable phonon polaritons in twisted α-MoO_3. *Nat. Mater.* **19**, 1307–1311 (2020). doi:10.1038/s41563-020-0732-6 Medline

29. J. Chen, M. Badioli, P. Alonso-González, S. Thongrattanasiri, F. Huth, J. Osmond, M. Spasenović, A. Centeno, A. Pesquera, P. Godignon, A. Z. Elorza, N. Camara, F. J. García de Abajo, R. Hillenbrand, F. H. L. Koppens, Optical nano-imaging of gate-tunable graphene plasmons. *Nature* **487**, 77–81 (2012). doi:10.1038/nature11254 Medline

30. Z. Fei, A. S. Rodin, G. O. Andreev, W. Bao, A. S. McLeod, M. Wagner, L. M. Zhang, Z. Zhao, M. Thiemens, G. Dominguez, M. M. Fogler, A. H. Castro Neto, C. N. Lau, F. Keilmann, D. N. Basov, Gate-tuning of graphene plasmons revealed by infrared nano-imaging. *Nature* **487**, 82–85 (2012). doi:10.1038/nature11253 Medline

31. G. Álvarez-Pérez, A. González-Morán, N. Capote-Robayna, K. V. Voronin, J. Duan, V. S. Volkov, P. Alonso-González, A. Y. Nikitin, Active tuning of highly anisotropic phonon polaritons in van der Waals crystal slabs by gated graphene. *ACS Photonics* **9**, 383–390 (2022). doi:10.1021/acsphotonics.1c01549

32. Y. Zeng, Q. Ou, L. Liu, C. Zheng, Z. Wang, Y. Gong, X. Liang, Y. Zhang, G. Hu, Z. Yang, C.-W. Qiu, Q. Bao, H. Chen, Z. Dai, Tailoring Topological Transitions of Anisotropic Polaritons by Interface Engineering in Biaxial Crystals. *Nano Lett.* **22**, 4260–4268 (2022). doi:10.1021/acs.nanolett.2c00399 Medline

33. F. L. Ruta, B. S. Y. Kim, Z. Sun, D. J. Rizzo, A. S. McLeod, A. Rajendran, S. Liu, A. J. Millis, J. C. Hone, D. N. Basov, Surface plasmons induce topological transition in graphene/α-MoO_3 heterostructures. *Nat. Commun.* **13**, 3719 (2022). doi:10.1038/s41467-022-31477-z Medline

34. H. Hu, N. Chen, H. Teng, R. Yu, Y. Qu, J. Sun, M. Xue, D. Hu, B. Wu, C. Li, J. Chen, M. Liu, Z. Sun, Y. Liu, P. Li, S. Fan, F. J. García de Abajo, Q. Dai, Doping-driven topological polaritons in graphene/α-MoO_3 heterostructures. *Nat. Nanotechnol.* **17**, 940–946 (2022). doi:10.1038/s41565-022-01185-2 Medline

35. G. Álvarez-Pérez, J. Duan, J. Taboada-Gutiérrez, Q. Ou, E. Nikulina, S. Liu, J. H. Edgar, Q. Bao, V. Giannini, R. Hillenbrand, J. Martín-Sánchez, A. Y. Nikitin, P. Alonso-González, Negative reflection of nanoscale-confined polaritons in a low-loss natural medium. *Sci. Adv.* **8**, eabp8486 (2022). doi:10.1126/sciadv.abp8486 Medline

36. P. Alonso-González, A. Y. Nikitin, F. Golmar, A. Centeno, A. Pesquera, S. Vélez, J. Chen, G. Navickaite, F. Koppens, A. Zurutuza, F. Casanova, L. E. Hueso, R. Hillenbrand, Controlling graphene plasmons with resonant metal antennas and spatial conductivity patterns. *Science* **344**, 1369–1373 (2014). doi:10.1126/science.1253202 Medline

37. P. Li, I. Dolado, F. J. Alfaro-Mozaz, F. Casanova, L. E. Hueso, S. Liu, J. H. Edgar, A. Y. Nikitin, S. Vélez, R. Hillenbrand, Infrared hyperbolic metasurface based on nanostructured van der Waals materials. *Science* **359**, 892–896 (2018). doi:10.1126/science.aaq1704 Medline

38. Y. Zhang, T.-T. Tang, C. Girit, Z. Hao, M. C. Martin, A. Zettl, M. F. Crommie, Y. R. Shen, F. Wang, Direct observation of a widely tunable bandgap in bilayer graphene. *Nature* **459**, 820–823 (2009). doi:10.1038/nature08105 Medline

39. D. J. Rizzo, B. S. Jessen, Z. Sun, F. L. Ruta, J. Zhang, J.-Q. Yan, L. Xian, A. S. McLeod, M. E. Berkowitz, K. Watanabe, T. Taniguchi, S. E. Nagler, D. G. Mandrus, A. Rubio, M. M. Fogler, A. J. Millis, J. C. Hone, C. R. Dean, D. N. Basov, Charge-Transfer Plasmon Polaritons at Graphene/α-$RuCl_3$ Interfaces. *Nano Lett.* **20**, 8438–8445 (2020). doi:10.1021/acs.nanolett.0c03466 Medline

40. F. J. García de Abajo, Graphene plasmonics: Challenges and opportunities. *ACS Photonics* **1**, 135–152 (2014). doi:10.1021/ph400147y

41. Y. Qu, N. Chen, H. Teng, H. Hu, J. Sun, R. Yu, D. Hu, M. Xue, C. Li, B. Wu, J. Chen, Z. Sun, M. Liu, Y. Liu, F. J. García de Abajo, Q. Dai, Tunable Planar Focusing Based on Hyperbolic Phonon Polaritons in α-MoO_3. *Adv. Mater.* **34**, 2105590 (2022). doi:10.1002/adma.202105590

42. J. Martín-Sánchez, J. Duan, J. Taboada-Gutiérrez, G. Álvarez-Pérez, K. V. Voronin, I. Prieto, W. Ma, Q. Bao, V. S. Volkov, R. Hillenbrand, A. Y. Nikitin, P. Alonso-González, Focusing of in-plane hyperbolic polaritons in van der Waals crystals with tailored infrared nanoantennas. *Sci. Adv.* **7**, eabj0127 (2021). doi:10.1126/sciadv.abj0127 Medline

43. J. Duan, G. Álvarez-Pérez, A. I. F. Tresguerres-Mata, J. Taboada-Gutiérrez, K. V. Voronin, A. Bylinkin, B. Chang, S. Xiao, S. Liu, J. H. Edgar, J. I. Martín, V. S. Volkov, R. Hillenbrand, J. Martín-Sánchez, A. Y. Nikitin, P. Alonso-González, Planar refraction and lensing of highly confined polaritons in anisotropic media. *Nat. Commun.* **12**, 4325 (2021). doi:10.1038/s41467-021-24599-3 Medline

44. Z. Zheng, J. Jiang, N. Xu, X. Wang, W. Huang, Y. Ke, S. Zhang, H. Chen, S. Deng, Controlling and Focusing In-Plane Hyperbolic Phonon Polaritons in α-MoO_3 with a Curved Plasmonic Antenna. *Adv. Mater.* **34**, 2104164 (2022). doi:10.1002/adma.202104164